1 **Correcting for water vapor diffusion in air bag samples for**

2 **isotope composition analysis: case~~s studies~~ study with drone-**

3 **collected samples**

4 Di Wang[1,2,3*], Camille Risi[2], Lide Tian[1], Di Yang[1], Gabriel J. Bowen[4], Siteng Fan[2,5],

5 Yang Su[6] , Hongxi Pang[7], Laurent Z.X Li[2]

6 *[1] Institute of International Rivers and Eco-security, Yunnan University, Yunnan Key*

7 *Laboratory of International Rivers and Transboundary Eco–security, Kunming 650500,*

8 *Yunnan, China*

9 *[2] Laboratoire de Météorologie Dynamique, IPSL, CNRS, Sorbonne Université, Campus*

10 *Pierre et Marie Curie, Paris 75005, France*

11 *[3] Laboratoire Atmosphères, Observations Spatiales, IPSL, CNRS, UVSQ, Sorbonne*

12 *Université, Guyancourt 78280, France*

13 *[4] Department of Geology and Geophysics, University of Utah, Salt Lake City, Utah 84108,*

14 *USA*

15 *[5] Department of Earth and Space Sciences, Southern University of Science and Technology,*

16 *Shenzhen 518055, China*

17 *[6] Département d'Informatique, École normale supérieure – PSL, 45 Rue d'Ulm, 75005*

18 *Paris, France*

19 *[7] Key Laboratory of Coast and Island Development of Ministry of Education, School of*

20 *Geography and Ocean Science, Nanjing University, Nanjing 210023, China*

21 **Corresponding author: di.wang@latmos.ipsl.fr*

Abstract

Mass spectrometry and laser spectroscopy, have been widely employed for precise water vapor isotope measurements. Nevertheless, these techniques are limited by logistical challenges in fieldwork, consequently constraining the temporal and spatial resolution of measurements. Specifically, water vapor isotope measurements are primarily limited to near-surface levels, while measurements in the free troposphere are notably scarce. Portable sampling devices, such as air bags and glass bottles, have therefore become necessary alternatives for collecting, storing, and transporting gaseous samples in diverse environments prior to analysis with less portable instruments. In drone-based high-altitude vapor sampling, air bags are preferred for their lighter weight and greater flexibility compared to glass bottles. Nevertheless, they present specific challenges, such as potential sample contamination and isotopic fractionation during storage, primarily due to the inherent permeability of air bags. Here, we developed a theoretical model for water vapor diffusion through the sampling bag surface, with parameters calibrated through laboratory experiments. This model enables the reconstruction of the initial isotopic composition of sampled vapor based on measurements obtained within the bag and from the surrounding environment. This diffusion model underwent rigorous validation through experiments conducted under varying humidity and isotopic composition differences between the inside and outside of the air bag, confirming its reliability. We applied this correction method to air samples collected at various pressures up to the upper troposphere using an air bag-mounted drone that we developed, thereby estimating the initial isotopic composition and uncertainty based on our observations. The corrected observations closely match the Picarro in-suit situ observations and IASI satellite retrievals. Our correction method significantly enhances the reliability and applicability of water vapor isotope observations conducted using drones equipped with air bags, and provides a detailed assessment of all potential sources of error and quantifies the uncertainty range of the observations. This approach leverages the strengths of drone-based air bag sampling while mitigating its limitations, thus facilitating the convenient collection of isotopic data throughout the troposphere.

1   Introduction

Water vapor isotopes provide unique insights into the transport, mixing, and phase changes of water in the environment, which are crucial for improving understanding of the climate system, hydrological cycle, atmospheric dynamics, and paleoclimate proxies. Water isotopes have also been applied in climate modeling, weather prediction, and water resource management (Bowen et al., 2019; Galewsky et al., 2016; Gat, 1996; West et al., 2009).

Water isotope analysis has traditionally relied on mass spectrometry, which, while accurate (Ghosh and Brand, 2003; Muccio and Jackson, 2009), demands labor-intensive preparation and lacks portability (West et al., 2010). Methods like cryogenic trapping effectively collect water vapor (Grootes and Stuiver, 1997; Michener and Lajtha, 2008; Steen-Larsen et al., 2011; Yu et al., 2015), but they require long sampling periods, limiting observation scope and timing. Over the past three decades, laser spectroscopy methods such as Cavity Ring-Down Spectroscopy (CRDS)(Hodges and Lisak, 2006) and Off-Axis Integrated Cavity Output Spectroscopy (OA-ICOS) (Johnson et al., 2011) have emerged, delivering a best-in-class combination of speed, high precision, and continuous measurements even in challenging environments such as high altitudes or arid regions with low water vapor content. Advances in these instruments have significantly expanded the field of water isotope research. However, their heavy instrumentation, substantial power requirements, and limited mobility restrict their usability in certain situations, particularly for aerial water vapor isotope measurements, which require lightweight and flexible sampling approaches. As a result, the collection and storage of physical samples are still necessary, increasing the demand for more convenient and efficient sample acquisition methods. Air bags and glass bottles have been practical solutions for collecting, storing, and transporting gaseous samples from various settings (Rozmiarek et al., 2021).

Given that air bags can reduce the weight of sampling equipment and increase sampling flexibility, there is considerable interest in using them for vapor sample collection. This is particularly advantageous for small equipment like drones, where minimizing payload weight is essential for sampling at high altitudes or over long distances. This selection also makes it easier to transport samples and reduces the risk of breakage. However, concerns have arisen regarding the suitability of various sampling materials for storing these samples, primarily due to potential water diffusion through container walls. Diffusion issues are commonly observed in sampling bags during water vapor isotope analysis and have persisted as a longstanding challenge in the field (Gralher et al., 2021; Havranek et al., 2020; Herbstritt et al., 2023; Magh et al., 2022). In previous studies, this issue is particularly concerning in the Direct Vapor Equilibrium Laser Spectroscopy (DVE-LS) method, which has been widely used to rapidly collect and measure water isotopes in evaporation-prone soil, rock, or plant samples. The DVE-LS method simplifies preparation and increases sample throughput by directly analyzing the vapor phase, thus eliminating the need for extensive physical extractions (Gralher et al., 2021; Hendry et al., 2015; Millar et al., 2018; Sprenger et al., 2015; Wassenaar et al., 2008). However, water vapor molecules may exchange between the air inside the bag and the external ambient air during sample storage. Water vapor molecules typically diffuse from areas of high humidity to drier areas. In this process, heavier isotopologues (e.g., $H_2^{18}O$ and HDO) move more slowly than lighter isotopologues (e.g., $H_2^{16}O$) due to their greater mass, resulting in preferential

diffusion of lighter isotopes. This differential diffusion, can alter the original isotopic composition of the collected air samples. Moreover, differential diffusion can also occur due to gradients in isotopic composition.

To mitigate these issues, specific diffusion-tight materials are highly recommended~~materials with lower permeability are suggested~~ for water vapor isotope measurements, although adsorption effects may still occur with such materials (Herbstritt et al., 2023). Further research and development are still necessary. This may involve exploring alternative materials for more impermeable sampling bags, improving sealing methods to better isolate sampled air, and developing sampling techniques less susceptible to diffusion. Resolving these issues is essential for ensuring the reliability of water vapor isotope measurements using air bags and for accurately understanding atmospheric and hydrological processes.

In light of the ongoing development and further refinement of these techniques and the associated cost constraints, we developed a diffusion model with parameters calibrated through laboratory experiments. This model is capable of assessing the permeability of the air bags and correcting the obtained isotope measurements to the initial pre-diffusion values based on the humidity, isotope values inside and outside the bag, and the sample storage time. This diffusion model was validated through experiments under varying humidity and isotopic composition differences between the inside and outside of the air bag, confirming its reliability. Furthermore, we also applied this diffusion method to air samples collected at different altitudes using a drone-based atmospheric vapor sampling device we developed, to estimate the initial isotope composition and uncertainty. The primary objective of this drone-based field campaign is to obtain atmospheric water vapor isotope data along vertical profiles in the troposphere, providing higher temporal and spatial resolution than satellite observations. The corrected near-surface drone-based measurements using our diffusion model show consistency with direct, in-situ surface-level measurements using the Picarro analyzer. Similarly, at two mid-tropospheric levels, the corrected drone measurements align with IASI satellite observations of water vapor isotopic composition, further confirming the model's theoretical and ~~practical~~ reliability in applications. However, because of the short residence time at high altitudes, the reduced diffusivity at low temperatures, and the flexibility of the bags maintaining equal internal and external pressure, our current approach does not explicitly resolve potential temperature- or pressure-dependent changes in bag permeability. Under our experimental conditions, these effects were instead addressed indirectly through conservative uncertainty estimates. Future applications should take into account the specific experimental conditions, and future developments may extend the model to explicitly incorporate the dependence of bag permeability on partial pressure and temperature, thereby improving its applicability under a wider range of atmospheric conditions.

2 Theoretical basis of diffusion model

2.1 Diffusion model description

Storing vapor samples in air bags prior to isotope measurement may alter the isotopic composition of the water vapor. The main reason is the diffusion of water molecules between

the interior and exterior of the air bags, primarily due to the permeability of the bag materials. We present a mathematical model for the diffusion and fractionation of isotopes across the surface of the sampling bag. In this model, we assume the ambient vapor flux entering the air bag changes the internal humidity and vapor isotopic composition, influenced by the different humidity and water isotopic composition inside and outside the bag (Fig.1).

The flux of water into the bag, F (in kg/m²/s), is expressed as:

$$F = k * (q_e - q(t)) \tag{1}$$

where $q(t)$ represents the variation of humidity inside the air bag over time (in kg/kg), q_e denotes the environmental humidity (in kg/kg), k is water vapor conductance. This first-order formulation is derived from Fick's diffusion law(Fick, 1855).

Similarly, the flux of isotopologue, F_i, either $H_2^{18}O$ or HDO, moving into the bag can be described as:

$$F_i = k_i * (R_e * q_e - R(t) * q(t)) \tag{2}$$

In this equation, k_i represents the conductance specific to each isotopologue (in kg/m²/s), R_e denotes the isotopic ratio in the environment, and $R(t)$ is the variation of isotopic ratio within the air bag with time. Notably, the fractionation coefficient here can be denoted as:

$$\alpha = \frac{k}{k_i} \tag{3}$$

Since k represents the total flux including both light and heavy molecules, it is approximated as the conductance of the heavy molecules (k_{heavy}), so that Eq. (3) is consistent with the conventional definition of fractionation factors ($\alpha = \frac{k_{heavy}}{k_{light}}$).

The validity of Eqs.1 and 2 relies on the assumptions that internal and external pressures remain equal to atmospheric pressure, ensuring no pressure gradient across the bag membrane, that the internal vapor is well-mixed, and that the exchange rate follows a first-order process. Additionally, if the temperature remains constant, k and k_i are assumed to be constant.

Assuming that diffusion through the bag is the primary transport mechanism, and neglecting adsorption, the temporal change in humidity can be modeled by the following differential equation:

$$\frac{d(q(t)*M)}{dt} = F * A \tag{4}$$

where A represents the exchange area (surface area of the air bag), and M is the air mass inside the bag.

Assuming that M is constant, which is reasonable given that the total mass variation due to water vapor flux is at most 1%, this equation simplifies to:

$$\frac{dq(t)}{dt} = \frac{F*A}{M} = \frac{k*A}{M} * (q_e - q(t)) \tag{5}$$

Here, we define the water vapor exchange coefficient as follows, it describes the rate at which water vapor exchanges across the bag membrane:

$$\lambda = \frac{k*A}{M} \tag{6}$$

Similarly, the temporal change in isotopic ratio can be modeled by the following differential equation:

171 $$\frac{d(R(t)*q(t)*M)}{dt} = M * (q(t) * \frac{dR(t)}{dt} + R(t) * \frac{dq(t)}{dt})$$

172 $$= F_i * A = k_i * (R_e * q_e - R(t) * q(t)) * A \qquad (7)$$

173 This equation can be simplified as:

174 $$\frac{dR(t)}{dt} = \frac{k_i*(R_e*q_e - R(t)*q(t))*A/M - R(t)*\frac{dq(t)}{dt}}{q(t)}$$

175 $$= \frac{\frac{k*A}{M*\alpha}*(R_e*q_e - R(t)*q(t)) - R(t)*\frac{k*A}{M}*(q_e - q(t))}{q(t)}$$

176 $$= \frac{\frac{\lambda}{\alpha}*(R_e*q_e - R(t)*q(t)) - R(t)*\lambda*(q_e - q(t))}{q(t)}$$

177 $$= \frac{\lambda}{\alpha} * (R_e - R(t)) + \frac{\lambda}{q(t)} * (q_e - q(t)) * (\frac{R_e}{\alpha} - R(t)) \qquad (8)$$

178

179 If q_e is stable (the environment is treated as an infinite reservoir), and that k and A are
180 constant, the differential equation for humidity (Eq. 5) can be analytically solved:

181 $$q_e - q(t) = (q_e - q_0) * e^{(-\frac{k*A}{M}*t)} = (q_e - q_0) * e^{(-\lambda*t)} \qquad (9)$$

182 where q_0 is the initial humidity at t = 0. This equation can also be expressed in terms of
183 natural logarithms as:

184 $$\ln(q_e - q(t)) = \ln(q_e - q_0) - \lambda * t \qquad (10)$$

185 Consequently, the slope of $\ln(q_e - q(t))$ against time is λ.

186

187 For the isotopic ratio, the analytical solution is only feasible when the initial humidity
188 equals the environmental humidity ($q_0 = q_e$):

189 $$\frac{dR(t)}{dt} = \frac{k*A}{M*\alpha} * (R_e - R(t)) \qquad (11)$$

190 Assuming that R_e, q_e, k, α and A are constant:

191 Thus, $$R_e - R(t) = (R_e - R_0) * e^{(-\frac{k*A}{M*\alpha}*t)} \qquad (12)$$

192 where R_0 denotes the initial isotopic ratio at t = 0. Again, taking the natural logarithm, we
193 obtain:

194 $$\ln(R_e - R(t)) = \ln(R_e - R_0) - \frac{\lambda}{\alpha} * t \qquad (13)$$

195 This equation demonstrates that the slope of $\ln(R_e - R(t))$ against time is the water vapor

196 isotopic exchange coefficient $\frac{\lambda}{\alpha}$. Knowing λ, we can deduce the isotopic fractionation

197 coefficient ~~due to fractionation caused by mass flow through bags,~~ α, for each isotope.
198 However, when the environmental humidity differs from the initial humidity inside the air
199 bag, a numerical solution is required to solve the differential equation for R (Eq. 8).
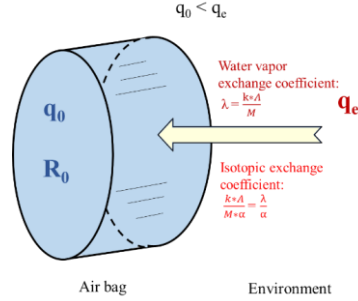
Figure 1 Schematic illustrating the diffusion model. q_0 represents the initial humidity in the air bag at t = 0, q_e denotes the environmental humidity, R_0 indicates the initial isotopic ratio in the air bag at t = 0, R_e represents the isotopic ratio in the environment, k is water vapor conductance, A denotes the exchange area (surface area of the bag), and M is the mass of air within the bag, and α denotes the isotopic fractionation coefficient.

2.2 **Reconstructing initial water vapor isotopic compositions**

The isotopic composition of the air bag water vapor undergoes an exponential evolution over time (Eq. 12). This method of applying exponential evolution equations to reconstruct isotopic compositions has been used in environmental forensics to investigate shifts in water isotopes due to metabolic changes, environmental conditions, or diet (Ayliffe et al., 2004; Cerling et al., 2006). Similarly, in climatology, this method helps retrieving initial isotopic composition from samples such as ice cores or tree rings, affected by evaporation, precipitation, and temperature fluctuations, facilitating historical climate reconstruction (Brienen et al., 2016). Here we apply a similar method, and apply the analytical solution of Eq.8 using data from experiments in which the condition that q_0 equals q_e is met to determine the equation parameters.

The constants (λ, $\alpha\_^{18}O$, $\alpha\_^2H$) can be determined through laboratory experiments and Eqs. 10 and 13 (see Subsection 3.2 and 4.1). If we know the initial values within the air bag (q_0, $R\_^{18}O_0$, $R\_^2H_0$), the ambient values (q_e, $R\_^{18}O_e$, $R\_^2H_e$) during storage (approximated using ground-level conditions) , and the storage time after sampling ($T\_{storage}$) of the sampling bag, we are able to simulate the variations in humidity and isotopic ratios inside the air bag according to Eqs. 5 and 8. Similarly, if we know $T\_{storage}$, the humidity and isotopic composition at time t = $T\_{storage}$ ($q_{(T\_storage)}$, $R\_^{18}O_{(T\_storage)}$, $R\_^2H_{(T\_storage)}$) in the air bag, and the ambient values, we can deduce the initial values in the air bag at t = 0 by back-calculating. The equation used for reconstructing the initial isotope ratio (R_0) is:

$$R_0 = R_{measured} - \int_0^{T_{storage}} \frac{dR(t)}{dt} dt$$

$$= R_{measured} - \int_0^{T_{storage}} (\frac{\lambda}{\alpha} * (R_e - R(t)) + \frac{\lambda}{q(t)} * (q_e - q(t)) * (\frac{R_e}{\alpha} - R(t))) \, dt \qquad (14)$$

where R_0 represents the initial isotopic ratio to be reconstructed, $R\_{measured}$ is the observed isotopic ratio after $T\_{storage}$, and $\frac{dR(t)}{dt}$ is defined in Eq. 8.

This approach allows us to correct for diffusion-induced isotopic shifts and reconstruct the

225 original vapor composition.

226   For mathematical clarity and consistency, isotopic ratios (R) are used in the equations
227 presented in previous sections. Replacing R with δ-values would only shift the physical basis
228 without affecting the mathematical validity of the equations or the estimation of α, as the
229 standard ratio cancels out. For clearer visualization, δ-values are used for numerical
230 applications and in the subsequent figures and tables.

231   The δ and d-excess values used in this study follow standard definitions:

232
$$\delta^{18}O \ = \left(\frac{R^{18}O_{sample}}{R^{18}O_{standard}} - 1 \right) * 1000 \qquad\qquad (15)$$

233
$$\delta^{2}H \ = \left(\frac{R^{2}H_{sample}}{R^{2}H_{standard}} - 1 \right) * 1000 \qquad\qquad (16)$$

234
$$d - excess = \ \delta^{2}H - 8 * \delta^{18}O \qquad\qquad (17)$$

235 Here, $R^{18}O_{standard} = 2.0052*10^{-3}$ and $R^{2}H_{standard} = 1.5576 * 10^{-4}$, corresponding to
236 the VSMOW international reference values.

3   Methods and data

3.1 Air bag isotope measurements
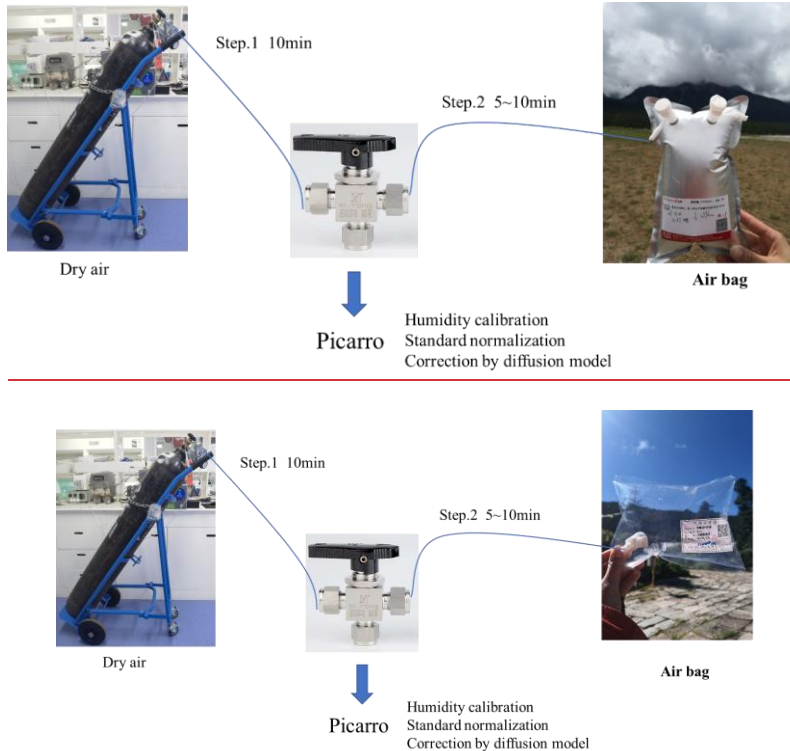
Figure 2 Setup for isotope measurements using air bags with a Picarro atmospheric water vapor isotope analyzer.

239   In this study, we used 0.5 L and 4L Teflon air bags produced by Dalian Hede Technologies
240   Co., Ltd to collect and store vapor, and measured the vapor isotopes using a Picarro 2130i water
241   isotope analyzer. Based on our testing and the airflow rate set for the Picarro analyzer, the 0.5
242   L and 4 L bags provided sufficient sample volume for approximately 17 minutes and 130
243   minutes of analysis, respectively.

244   Figure 2 illustrates the setup for measuring vapor isotopes in air bags. In this system, the
245   air inlet of the Picarro isotope analyzer was connected to a three-way valve through Teflon or
246   stainless-steel tubing. The other two ports of the three-way valve were attached to the outlet
247   valve of the air bag and a dry air cylinder, respectively. Sample storage and measurement were
248   conducted in a temperature-regulated room to maintain constant temperature conditions for the
249   air bags and tubing.

250   In the measurement procedure, we first activated the dry air cylinder and adjusted the
251   pressure reducing valve to 13.8 kPa (2 psi (,pounds of force per square inch), within the Picarro
252   water isotope analyzer's recommended range of 13.8–27.6 kPa (2–4 psi) for carrier gas. The
253   instrument's built-in flow regulation maintains a gas flow rate of 40 sccm at 760 Torr,
254   corresponding to ~ 30–50 mL/min in our measurement conditions, ensuring stable sample
255   delivery. We then opened the valve channel connecting the dry air cylinder to the three-way
256   valve, allowing dry air to flow into the isotope analyzer and flush all air pathways for 10
257   minutes. Subsequently, we closed the dry air channel, opened the air bag outlet valve, and the
258   corresponding valve channel on the three-way valve. This allowed water vapor in the air bags
259   to be analyzed at a constant temperature in the Picarro analyzer, a process lasting between 5
260   and 10 minutes. Upon completion, we switched the valve to measure dry air. By repeatedly
261   measuring isotopic composition for replicate samples—air samples collected simultaneously
262   under the same conditions—we ensured the consistency of achieved greater accuracy in the
263   water vapor measurements.

264   To correct isotope measurement bias caused by the instrument's sensitivity to different
265   water vapor concentrations (Schmidt et al., 2010), we used the built-in Standard Delivery
266   Module (SDM) of the Picarro L2130-i water vapor isotope analyzer to generate a 500–25,000
267   ppm water vapor gradient for isotope measurements. We selected 20,000 ppm as a reference
268   humidity level, as this corresponds to the optimal accuracy range of the Picarro analyzer
269   (JingfengLiu et al., 2014; Schmidt et al., 2010). All the measured vapor isotope data were
270   normalized to the VSMOW-SLAP scale using two distinct laboratory reference waters with
271   known isotopic composition. Before conducting daily measurements, we adjusted the quantity
272   of the injected liquid standard to align with the humidity of the external vapor measurements.

273   3.2 **Laboratory permeability experiments**

274   To evaluate the variations of the diffusion of water molecules between the interior and
275   exterior of the air bags, we conducted the following experiments (Table S1A1), as detailed
276   below:

3.2.1   Experiment No. 1: Quantification of $\lambda_{\_surface}$

To quantify the water vapor exchange coefficient at the surface, $\lambda_{\_surface}$, using Eq.10, we filled the empty and clean air bags with dry air and measured humidity variations using a Picarro analyzer at intervals of 1 minute, 2, 4, 6, 8, and 10 hours following the measurement method described in Subsection 3.1. As λ is related to the exchange area (surface area of the air bag), Mmeasurements were conducted using 0.5L and 4L air bags, with repetitions on both identical and different air bags of the same dimensions (refer to the experiment times in Table 1 and results in Fig.3a). We measured $\lambda_{\_surface}$ (=k*A/M) under near-surface pressure and temperature we set in a controlled chamber. While k may vary with temperature and pressure, these effects were assumed negligible within the condition of our study. Results will be shown in Subsection 4.1.

3.2.2   Experiment No. 2: Quantification of α

To investigate isotope variation patterns and improve measurement accuracy during storage in the air bag to quantify the isotopic fractionation coefficient, α, using Eq.13, initial values significantly different from ambient conditions were selected. Empty, clean air bags were first filled with dry air, then sealed by closing the bag valve. To maintain a closed system while injecting reference water, a dedicated injection septum was installed on the valve. After reopening the valve, a fixed amount of laboratory reference liquid water with known isotopic composition was injected into the dry air-filled bag using a 10 μL injection needle. In Experiment No. 2, we ensured that the initial humidity (q_0) was approximately equal to the environmental humidity (q_e). To ensure $q_0 = q_e$, the environmental vapor concentration was first measured, followed by the calculation and experimental determination of the water volume to be injected into the air bag. Water vapor concentration and isotope variations within the air bags were then measured using a Picarro analyzer at intervals of 5 minutes, 2, 4, 6, 8, and 10 hours. Results will be shown in Subsection 4.1. To ensure data consistency and reliability, we repeated these measurements multiple times using air bags of both the same and different sizes, including 0.5L and 4L bags. For the 0.5L air bags, a separate bag was prepared for each time interval, and water vapor concentration and isotopic compositions were measured once to ensure that the parameter M remained stable without being affected by repeated measurements. However, manual injection of reference water with known isotopic composition introduced some variability, causing minor variations in initial values across all bags. This is evident in Figs 5, 6, and S2A2, where $q_0 = 1/2\ q_e$ data exhibit slight fluctuations due to the use of separate bags for each time interval. To address this, we repeated the experiment with 4L air bags, measuring the same air bag at different time intervals, which ensured consistent initial conditions at t=0 but allowed M to change over time. When air bags differ only in size, the parameter λ associated with A and M varies, while the isotopic fractionation coefficient α is theoretically constant. Both approaches could contribute to uncertainties in the mismatches between the model and experimental results. Therefore, we incorporated the results from both the 0.5 L and 4 L experiments into our uncertainty estimation of these mismatches, as detailed in Subsections 3.2.3 and 3.4.2.

3.2.3 Experiment No. 3: Diffusion model validation

To validate the diffusion model under diverse conditions and evaluate its uncertainties, we repeated Experiment No. 2, but injected different amounts of water with known isotopic composition to achieve a range of humidities from approximately $1/8 * q_e$ to q_e. Using the method described in Experiment No. 2, we injected 6 to 50 μL of reference water into a 4L air bag filled with dry air to achieve the desired humidity range. Additionally, we repeated the experiment using two reference waters with distinct isotopic compositions, specifically $\delta^{18}O$ = -58.07‰, δ^2H = -447.41‰ and $\delta^{18}O$ = -29.84‰, δ^2H = -222.84‰. To assess extended-duration variations, we also lengthened the time interval to 24 hours.

Once the parameters of the diffusion model have been obtained through Experiments No. 1 and 2, we used this model to simulate the variations in water vapor humidity and isotopic composition inside the air bag over time for Experiments No. 2 and 3 (refer to Section 2). When simulating these experiments using the diffusion model, we used measurements taken after a 5-minute delay as the initial condition to ensure that it represented complete evaporation of the injected water. We then simulated the temporal variations in humidity and vapor isotopes within the air bag using a 5-minute time step using Eqs.5 and 8, separately. The resulting outputs (hereafter referred to as 'the diffusion model simulations') will be shown in Subsection 4.2 and code are available as supplementary material.

3.3 Drone-mounted systems and field campaign

We designed and built a collection module for fixed-height sampling, incorporating diaphragm vacuum pumps, a rudder mounted on the drone, and a control module linked to a remote operating system. Before flight, each air bag was evacuated on the ground using the diaphragm pumps. When inactive, these self-sealing pumps effectively isolated the interior of the air bags from the external environment, minimizing diffusion prior to sampling. When the drone reaches a specified altitude, we remotely activate the designated air pump to inflate a specific air bag. Once sampling is complete, the pump is deactivated, and the drone ascends to the next target altitude, where the corresponding air pump inflates another air bag. This process was repeated until all predetermined samples were collected. After each sampling, the pump remained sealed, ensuring no unintended air ingress during descent. Self sealing diaphragm vacuum pumps were used to transfer air into the sampling bags. Once the pump ceased operation, it remained sealed from the external environment, preventing unintended air ingress. Additionally, due to the flexible nature of the air bags, internal and external pressures remained balanced. As air pressure increases during the drone's descent after collection. To further prevent the loss of collected air samples, a one-way valve was installed to block backflow. Additionally, the one-way valve helps prevent large droplets from entering the air bag during the collection process.

The sampling module was mounted on our specially designed high-altitude drones and deployed during a field campaign conducted from June 25, 2020, to October 17, 2020, in the pristine forests of Mountain Laojun, Lijiang, on the southeastern edge of the Tibetan Plateau and the northwestern of the Yunnan-Guizhou Plateau, China. We collected water vapor samples

357 every 500 meters, starting from near the surface along the vertical profile. To optimize sampling
358 across different altitude ranges, we deployed UAVs designed for varying flight altitudes.
359 Generally, the UAV operating at lower altitudes collected samples at seven heights from 4,000
360 to 7,000 meters in a single flight. The mid-altitude UAV collected samples at four heights from
361 7,500 to 9,000 meters in one flight, while the high-altitude UAV collected samples at four
362 heights from 9,500 to 11,000 meters in two flights. Each flight took approximately 20~30
363 minutes. In case of any disruptions during sampling, we repeated the process until a complete
364 vertical profile was obtained. At the beginning of the experiment, we also collected replicate
365 samples at each height to ensure data consistency.

366 By integrating high-altitude drone sampling with subsequent water vapor isotope analysis
367 using the Picarro analyzer at the surface, we obtained vapor isotopic profiles up to an altitude
368 of 11 km. Unlike conventional methods, such as cryogenic vapor sampling, this approach
369 requires much less sample volume and allows for timely measurements. Additionally, compared
370 to large aircraft, airships, and balloon-based observations, this method is relatively low-cost
371 and supports more flexible and long-term observations.

3.4 Application of diffusion model to vertical profiles

3.4.1   Estimating the air mass in the bag

374 λ is defined as k*A/M and depends on the air mass M in the bag. In drone-based vertical
375 sampling, M varies with altitude due to pressure changes, requiring an estimate of λ for different
376 altitudes ($\lambda_{\_alt}$). However, since λ is an intrinsic property of the bag material, its apparent
377 variation reflects uncertainties in estimating collected M, which depend on atmospheric
378 pressure (P), sampling time, and pump efficiency (ε):

379 $$M_{\_alt} = M_{\_surface} * \frac{P_{\_surface}}{P_{\_alt}} * \frac{Sampling\ time_{\_alt}}{Sampling\ time_{\_surface}} * \varepsilon \qquad (15)$$

380 where M_{alt} is the air mass collected at a different altitude and $M_{\_surface}$ represents the air
381 mass collected at the surface. At higher altitudes, where the air pressure ($P_{\_alt}$) is lower than at
382 the surface ($P_{\_surface}$), less air will be pumped into the air bag. To compensate for this effect, a
383 longer sampling time was used to collect air at higher altitudes (Sampling time$_{\_alt}$) than at the
384 surface (Sampling time$_{\_surface}$) (Fig.A1).

385 Given that $\lambda_{\_alt}$ is proportional to $M_{\_alt}$, we calculated it as:

386 $$\lambda_{\_alt} = \lambda_{\_surface} * \frac{P_{\_surface}}{P_{\_alt}} * \frac{Sampling\ time_{\_alt}}{Sampling\ time_{\_surface}} * \varepsilon \qquad (16)$$

387 where $\lambda_{\_surface}$ is the λ quantified experimentally at the surface.

388 Since air pressure and sampling times were directly measured, the primary source of error
389 for $M_{\_alt}$, and consequently $\lambda_{\_alt}$, arises from pump efficiency (ε), which may decrease over time
390 and at lower pressures. Using the estimated $\lambda_{\_alt}$, the observed vertical isotope profiles were
391 corrected based on Eq.14 from Section 2.2. The uncertainty estimation is discussed in Section
392 3.4.2.

3.4.2 The method of uncertainty estimation

Potential errors in correcting vertical profiles using the diffusion model include estimates of λ_{surface}, α, pump efficiency (ε), and mismatches between model and experiments (Table 1). We detail each below:

1) λ_{surface} uncertainty: laboratory experiments provided upper and lower bounds on λ_{surface} (Subsection 4.1). These were used for error estimation.

2) α uncertainty: the λ and λ/α were first estimated from several experiments, from which α was calculated. Their averaged values were used separately to parameterize the model. As highlighted in Subsection 3.2.2, estimating λ/α (and subsequently calculating α) requires results from cases where q_0 equals q_e, minor variations in q_0 and fluctuations in q_e could introduce non-systematic discrepancies between the model and experimental results. Consequently, for analyzing the contribution of α to uncertainties, only α derived from experiments where the model closely matched the majority of experimental results were considered. Selection criteria for these experiments included minimal deviation between q_0 and q_e, minimal deviation between experimental data and simulations, and stable q_e, ensuring the reliability of the chosen α.

3) Pump efficiency (ε) uncertainty: The efficiency of the pump may decline over time or vary with atmospheric pressure, affecting the collected air mass M. To account for this, we applied a conservative uncertainty range of 0.75 to 1.25 relative to surface conditions, ensuring the full range of possible variations in M_{alt} was considered.

4) Model-experiment mismatches: We compared model simulations with experimental data across 87 cases, calculating the average absolute discrepancy. These mismatches were included as an additional uncertainty component.

Total Uncertainty Calculation: The maximum discrepancy across all calibration results—using the full uncertainty range for λ_{surface}, α, and pump efficiency (ε)—was determined. The model-experiment mismatch was then added as an independent error component. The final uncertainty estimates, reported in Subsections 4.3 to 4.5, account for all potential error.

Table 1 Uncertainties and estimation methods

Uncertainties	Number of experiments	Estimation method	Used value (min~max for error estimation)
$\lambda_{\_surface}$	7 (0.5L bags); 6 (4L bags)	Obtained from lab experiments (max & min)	For 0.5L air bags: 0.031(0.0291~0.0317); For 4L air bags: 0.0255(0.0250~0.0259)
α	4	Obtained from lab experiments	$\alpha\_^{18}O$ is 1.0241, $\alpha\_^{2}H$ is 1.0451 ($\alpha\_^{18}O$ is 1.0254, $\alpha\_^{2}H$ is 1.0506 and $\alpha\_^{18}O$ is 1.0264, $\alpha\_\delta^{2}H$ is 1.0380)
Pump efficiency (ε)	-	0.75~1.25 relative to surface conditions	0.75~1.25
Mismatches between model and experiments	87	Average of all differences between experimental data and simulations	0.5 ‰ for $\delta^{18}O$, 4.1 ‰ for $\delta^{2}H$, 2.9 ‰ for d-excess

421   ### 3.5 Satellite isotope data from IASI

422   Several satellite missions have contributed to water vapor isotope observations, including
423   the Tropospheric Emission Spectrometer (TES) onboard Aura (2004–2018) (Worden et al.,
424   2006), the Scanning Imaging Absorption Spectrometer for Atmospheric Cartography
425   (SCIAMACHY) onboard Envisat (2002–2012), the Atmospheric Infrared Sounder (AIRS)
426   onboard Aqua (since 2002) (Worden et al., 2019), and the Tropospheric Monitoring Instrument
427   (TROPOMI) onboard Sentinel 5 Precursor (since 2017) (Schneider et al., 2022). In this study,
428   we use the MUSICA retrievals from the Infrared Atmospheric Sounding Interferometer (IASI)
429   onboard METOP due to its broad spatiotemporal coverage, vertical profiling capability, and the
430   availability and accessibility of its dataset (Diekmann et al., 2021). It has a horizontal footprint
431   of approximately 12 km at nadir (directly below the satellite), increasing with the angle of
432   observation. This configuration ensures nearly global coverage twice daily.
433   In this study, as no satellite retrievals of $\delta^{18}O$ are currently available, we compared our
434   observed vapor $\delta^{2}H$ profiles up to the upper troposphere with satellite observations. Due to the
435   intermittent availability of IASI data at any given location, we limited our comparison of
436   observational results across various altitudes at our study site to days when IASI data were
437   available. Satellite measurements, particularly for vertical profiles of water vapor isotopes, are
438   inherently different from direct sampling, they represent a vertical average over layers
439   determined by the averaging kernels (Rodgers and Connor, 2003; Worden et al., 2006).
440   Therefore, their comparability with ground-based or drone-based observations, which provide
441   high-resolution local data, is limited. The MUSICA retrievals from the IASI satellite instrument
442   provides water vapor isotope data at three altitude levels: 1-3 km in the lower troposphere, 4-7
443   km in the mid-troposphere, and 8-12 km in the upper troposphere. Given that our study started
444   at an altitude of 3856 m, we used the retrieved $\delta^{2}H$ data for the 4–7 km and 8–12 km levels.
445   However, these measurements represent a vertical average over layers determined by the

446 averaging kernels (Rodgers and Connor, 2003; Worden et al., 2006). While using averaging
447 kernels to smooth the observed profile could facilitate a more quantitative analysis, we simply
448 averaged the observations for the corresponding altitudes. Consequently, the comparison
449 remains mainly qualitative.

4 Results

4.1 Parameter estimates

452 The $\lambda_{surface}$ was determined through laboratory Experiment No. 1. Based on Eq.10, the
453 parameter $\lambda\_surface$ was estimated to be 0.0312 (uncertainty range: 0.0291 to 0.0317) for the
454 0.5 L air bags and 0.0255 (uncertainty range: 0.0250 to 0.0259) for the 4 L air bags (Fig. 3a,
455 Table 1).
456 The isotopic fractionation coefficients, α, were determined through laboratory Experiment
457 No. 2. From the averaged results of these measurements, using Eq.13, the water vapor isotopic
458 exchange coefficient, expressed as λ/α, was estimated to be 0.0249 for ^{18}O and 0.0244 for ^2H
459 (Fig. 3b and c). Consequently, $\alpha\_^{18}O$ was estimated to be 1.0241 (0.0255/0.0249), and $\alpha\_^2H$
460 was estimated to be 1.0451 (0.0255/0.0244) (Fig. 3b and d). Two additional sets of fractionation
461 coefficients, α, were obtained: $\alpha\_^{18}O = 1.0254$, $\alpha\_^2H = 1.0506$, and $\alpha\_^{18}O = 1.0264$, $\alpha_^2H = $
462 1.0380 (Table 1).
463 The specific parameter values obtained in this study pertain to the Teflon air bags used in
464 the aforementioned tests, conducted at an ambient temperature of 16°C. These values depend
465 on bag material, temperature, and pressure, which should be considered when applying the
466 model under different conditions. We also noted batch-to-batch variations among air bags from
467 the same manufacturer. We apply α measured under ground-level storage and measurement
468 conditions, assuming negligible temperature and pressure effects during the short (10–20 min)
469 drone-based sampling period. Future work is needed to quantify these dependencies.

470
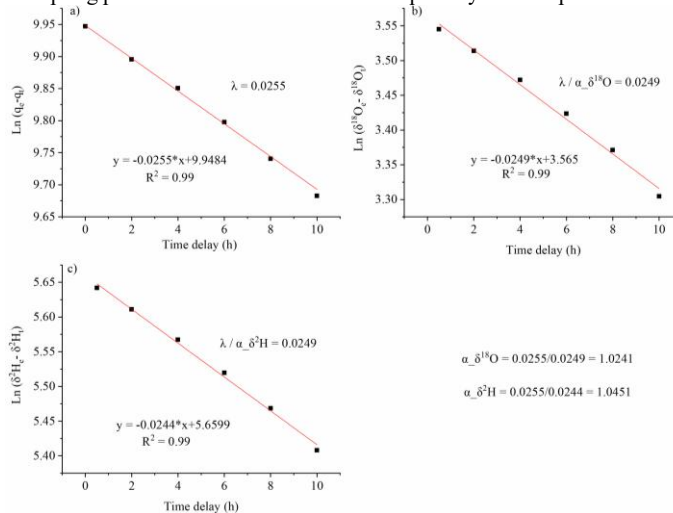
Figure 3 Determination of 3 parameters of the diffusion model : λ_surface (a) from Experiment No. 1, α_^{18}O// (b), and α_^{2}H (c) from Experiment No. 2.

4.2 **Diffusion model validation**

4.2.1   General case
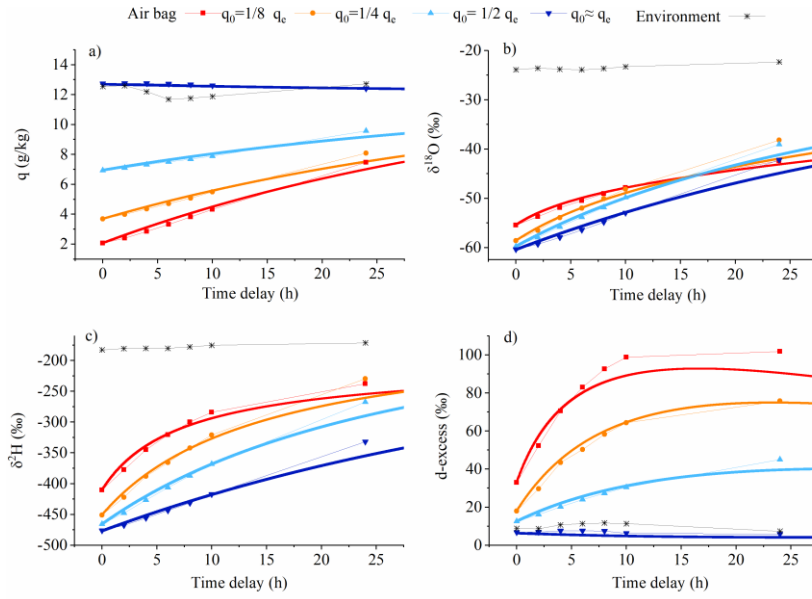
*Figure 4: Comparison of the variation within the air bag over time in laboratory permeability experiments (markers) and diffusion model simulations (lines) across a range of initial humidities at t = 0 (q_0), ranging from approximately 1/8 * q_e to q_e (q_e denotes the environmental humidity), under the condition that the water vapor isotopic composition in the air bag significantly differs from ambient values : a) humidity; b) $\delta^{18}O$; c) δ^2H, d) d-excess.*

To validate the model, we used Experiment No.3 described in Subsection 3.2. The diffusion model simulations (lines in Figs. 4, 5, 6, and Fig. ~~S2~~A2) are in close agreement with our experimental observations (markers in Figs. 4, 5, 6, and Fig. ~~S2~~A2), showing consistency in humidity, $\delta^{18}O$, δ^2H, and d-excess variations, with only minor deviations. Shorter storage times produce fewer deviations. When the humidity inside the air bag is lower than the ambient level, vapor from the environment enters the air bag, resulting in a gradual increase in humidity (Fig. 4a and Fig. ~~S2~~A2). Meanwhile, because the water vapor isotopic composition in the air bag is significantly lower than the ambient values, $\delta^{18}O$ and δ^2H in the air bag gradually increase and toward ambient values as ambient moisture enters the bags over time (Fig. 4b and c). In contrast, the d-excess increase as the time delay progresses due to kinetic fractionation during moisture diffusion into the air bag (Fig. 4d), as detailed in the following Subsection 4.2.2.

We observed that some curves unexpectedly intersect, which can be understood by

486   analyzing Eq. 8. The first term $(\frac{\lambda}{\alpha}*(R_e-R_{(t)}))$ continuously drives $R_{(t)}$ towards R_e, while the

487   second term $(\frac{\lambda}{q(t)}*(q_e-q_{(t)})*(\frac{R_e}{\alpha}-R_{(t)}))$ modulates the rate of change. Initially, for simulations

488   with lower q_0 (e.g., the red and orange curves), $q_e-q_{(t)}$ is large, making the second term
489   significant and positive, thereby increasing $R_{(t)}$ more rapidly. However, as $R_{(t)}$ exceeds R_e/α, the
490   sign of this term reverses, slowing down the increase in $R_{(t)}$ compared to other curves. In
491   contrast, curves with higher initial q_0 (e.g., blue curve) experience a steadier growth and
492   eventually surpass the initially faster-growing curves, leading to the observed crossing.

493   **4.2.2   Particular cases**

494
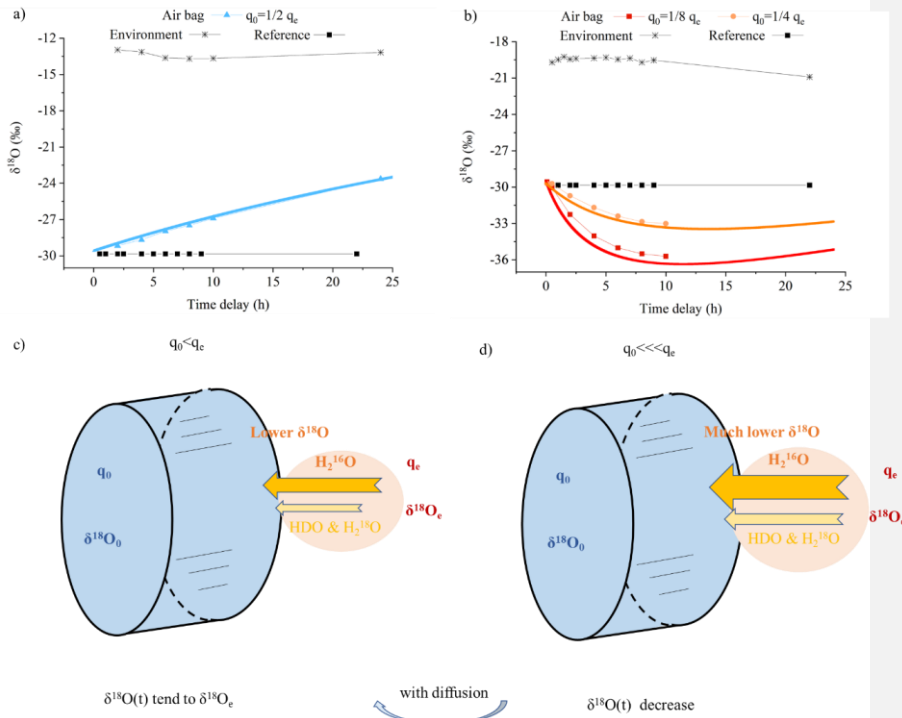
Figure 5   (a-b) Variations of $\delta^{18}O$ under different conditions: (a) when both the differences between internal ($\delta^{18}O_0$) and external ($\delta^{18}O_e$) $\delta^{18}O$ as well as between internal (q_0) and external (q_e) humidity are not significant, $\delta^{18}O$ gradually increases toward equilibrium; (b) when q_0 is significantly lower than q_e, a stronger vapor influx causes enhanced kinetic fractionation, leading to a decrease in $\delta^{18}O$. (c-d) Corresponding schematics: (c) illustrates the mechanism for (a), where a weaker humidity gradient results in slower isotopic shifts, while (d) corresponds to (b), showing intensified fractionation with a larger gradient, with arrows indicating vapor flux direction and fractionation intensity. $\delta^{18}O$ (t) is the variation of $\delta^{18}O$ within the air bag over time. In (a) and (b), the colored lines represent model simulations based

Due to isotopic kinetic fractionation, lighter $H_2^{16}O$ molecules preferentially diffuse into the air bag compared to heavier isotopologues such as $HD^{16}O$ and $H_2^{18}O$, resulting in a vapor flux with lower $\delta^{18}O$ relative to ambient vapor (Fig. 2). Moreover, variations within the air bag are driven by differences in water vapor content and isotopic ratios between its interior and exterior, as described in the diffusion model in Section 2. As shown in the initial experiment (Fig. 4b and c), when the internal $\delta^{18}O$ and δ^2H are significantly below the ambient values, the δ-values of the diffusing vapor, although lower than ambient, still exceeds the initial internal δ-values, leading to a gradual increase towards the ambient values; diffusion simply equilibrates the isotopic composition in the bag and the environment. When the disparity between internal and external $\delta^{18}O$ or δ^2H is not very substantial, and humidity differences are also minimal, the weaker diffusive gradient produces less net kinetic fractionation. This results in a small amount of vapor with lower $\delta^{18}O$ and δ^2H than the ambient moisture entering preferentially, but not falling below internal initial values, thereby still drives a progressive increase in the internal values towards ambient moisture (Fig. 5a and c). In contrast, with the same initial contrast between internal and ambient δ-values, that is, the disparity between internal and external $\delta^{18}O$ and δ^2H is less pronounced, but q_o is much lower than q_e, there is a stronger net flux into the bag, and this flux fractionates more rapidly; much more vapor with significantly lower $\delta^{18}O$ and δ^2H than the ambient moisture (and lower values than the initial internal vapor) enters the air bags and dominates their isotopic composition, thereby reducing the internal δ-values (Fig.5b and d). The smaller the difference in humidity and isotopic composition between the inside and outside of the air bag, the slower and smaller the isotopic change in the vapor within the air bag (Fig. 5 and Fig. 6).

517

518
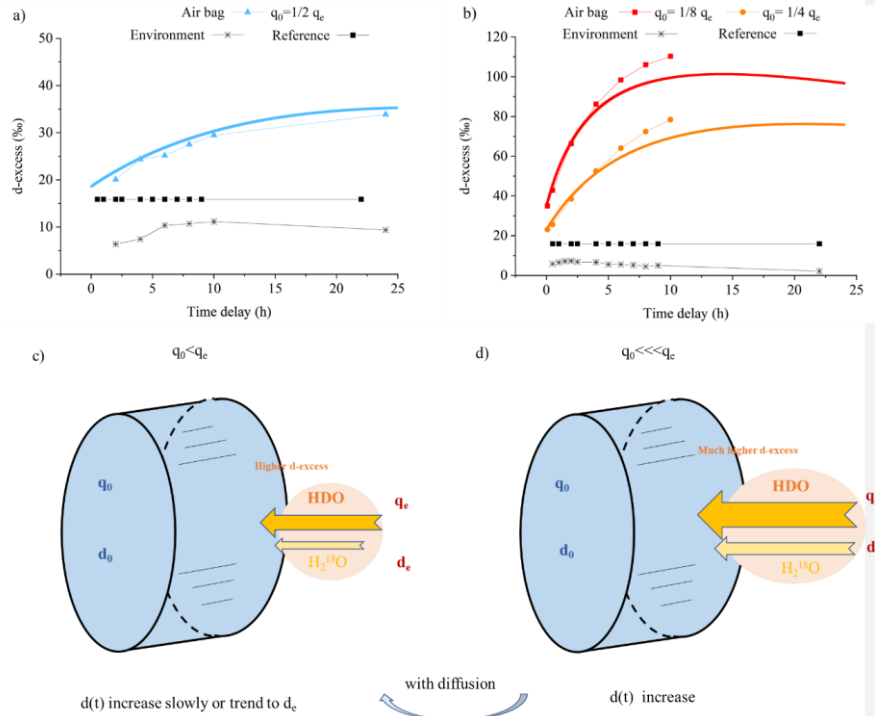
Figure 6 (a-b) Same as Fig.5, but showing the evolution of d-excess: (a) when the difference
519
between the humidity inside (q_0) and outside (q_e) the air bag is not significant, d-excess
520
increases gradually; (b) when q_0 is significantly lower than q_e, a stronger vapor influx
521
enhances kinetic fractionation, causing a more rapid d-excess increase. (c-d) Corresponding
522
schematics: (c) illustrates the mechanism for (a), where a smaller humidity gradient results in
523
slower isotopic shifts, while (d) corresponds to (b), showing intensified fractionation with a
524
larger gradient. d_0 indicates the initial d-excess at t = 0, d_e represents the d-excess in the
525
environment. d(t) denotes the variation of d-excess within the air bag over time.
526

In addition, because HDO and $H_2^{18}O$ diffuse at similar rates the magnitude of the kinetic
527
fractionation for D and ^{18}O is similar. However, since d-excess reflects deviations relative to
528
the 8:1 fractionation ratio typical of equilibrium processes, the tendency is for kinetic
529
fractionation during diffusion to contribute vapor with high d-excess and cause an increase in
530
d-excess during air bag storage as water vapor is added to the bag (Fig. 6a and c). When the
531
humidity difference between the inside and outside of the air bag increases, the d-excess of the
532
incoming vapor flux increases as a result of more intensive kinetic fractionation. This leads to
533
a faster increase in the vapor d-excess inside the air bag (Fig. 6b and d).
534

Regardless of the differences in water vapor humidity and isotopic compositions inside
535
and outside the air bag, the diffusion model simulations closely match the experimental
536
observations (Figs.4, 5 and 6). Using the method described in Subsection 3.4.2, the average
537
difference between all simulations and experimental data for each parameter represented the
538

539 model-experiment mismatch: 0.5 ‰ for $\delta^{18}O$, 4.1 ‰ for δ^2H, and 2.9 ‰ for d-excess.

540 ### 4.3 **Raw and corrected vertical profiles**

541 Here, we present a summary of drone-based observations from the field campaign at Mount
542 Laojun, Lijiang, on the southeastern edge of the Tibetan Plateau and the northwestern of the
543 Yunnan-Guizhou Plateau, China, conducted between June 25, 2020, and October 17, 2020.

544
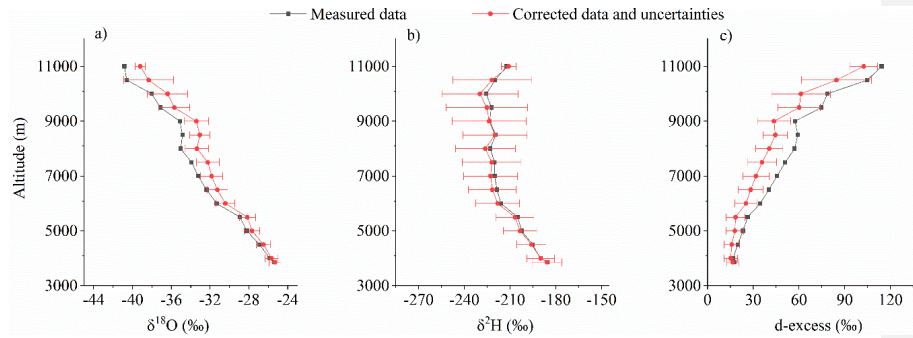
Figure 7 Comparison of vertical profiles for the mean values of all raw measurements
and corrected data from June to October, and associated uncertainties for $\delta^{18}O$ (a), δ^2H (b)
and d-excess (c).

545 As altitude increases, vapor $\delta^{18}O$ and δ^2H decrease due to condensation and precipitation
546 processes that occur as air masses ascend, which preferentially remove heavier isotopes
547 following Rayleigh distillation (Dansgaard, 1964). Meanwhile, the d-excess rises. This pattern
548 aligns with previous observations in the lower troposphere (He and Smith, 1999; Salmon et al.,
549 2019) and simulations of complete vertical profiles (Bony et al., 2008).
550 In our observations, the variation in $\delta^{18}O$ across the vertical profile from ground level at
551 3856 meters to 11 km is approximately 10-15‰. However, as altitude increases, the air becomes
552 progressively drier, leading to a greater disparity in humidity between the air collected in the
553 air bag and the surface storage environment. This aligns with the variations in Subsection 4.2.2
554 (Figs. 5b, 5d, and 6b, 6d). The strong kinetic fractionation driven by the diffusion of air into the
555 air bag results in a decrease in the water vapor $\delta^{18}O$ within the bag. After applying model
556 corrections, the corrected $\delta^{18}O$ inside the bag increased slightly compared to pre-correction
557 levels. As described in Subsection 4.2, vapor flux with higher d-excess entering the bag
558 increases the d-excess inside. As a compensation, the diffusion model applies corrections,
559 resulting in a reduced d-excess after correction (Fig. 7c and 10).

560 ### 4.4 **Uncertainty estimates**

561 According to the method of uncertainty estimation elaborated in Subsection 3.4.2, we
562 determined the ranges for four errors to evaluate uncertainty (Table 1).
563

564
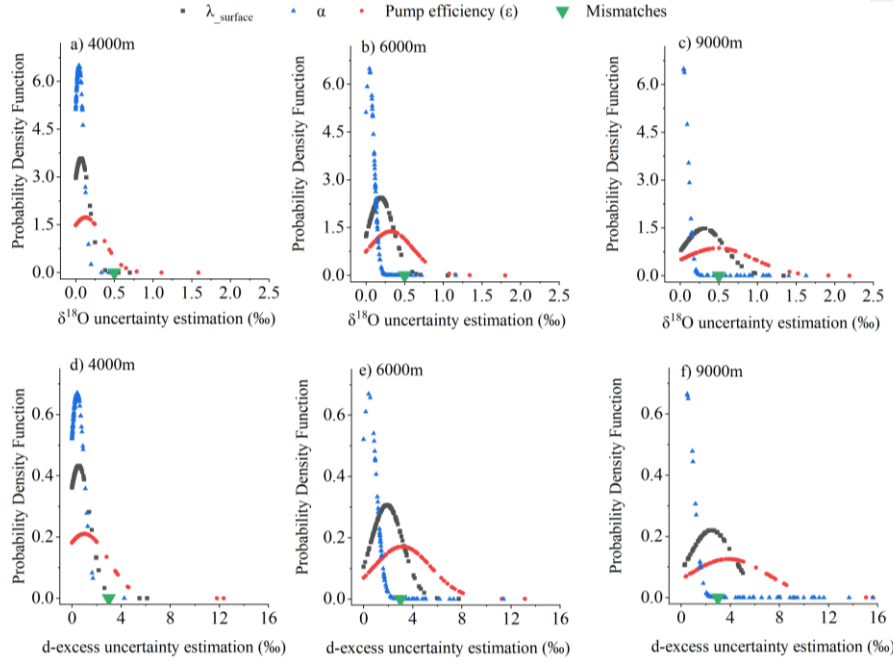
Figure 8: Contributions of different sources of uncertainty for δ¹⁸O (a, b, c for 4000m, 6000m, 9000m, respectively) and d-excess (d, e, f for 4000m, 6000m, 9000m, respectively). The green triangle shows the average mismatch between the model and experimental results. The peak position of each probability density function (PDF) represents the most likely uncertainty value for a given source, while the width of the distribution reflects the variability.

565   We representanalyzed the contributions of uncertainty sources to vertical vapor δ¹⁸O and
566   d-excess measurements at different altitudes using probability density function plots (Fig. 8).
567   Each PDF peak indicates the most probable uncertainty value, while its width reflects
568   sensitivity to that parameter. Narrow PDFs suggest stable, well-constrained uncertainty sources,
569   whereas broader PDFs indicate greater variability and a more diffuse impact on the correction
570   outcome. The mismatch between the model and the experiment (green marker), calculated
571   using the method described in Subsection 3.4.2, is assumed to remain constant across all
572   altitudes. The other three error sources manifest as unimodal normal distributions at various
573   altitudes for both δ¹⁸O and d-excess. Errors due to uncertainties in pump efficiency (ε) are the
574   main source, exhibiting the largest spread (Fig. 8) and increasing with altitude (Fig. 9). Errors
575   derived from $\lambda_{\_surface}$ and α also increase with altitude (Figs. 8 and 9). As a result, at higher
576   elevations, the satellite δ²H differs more from the measured and corrected data than at lower
577   altitudes (Fig. 10). This pattern arises because $\lambda_{\_alt}$ deviates more from $\lambda_{\_surface}$ at higher
578   elevations (Eq.16), primarily due to increased errors in estimating $M_{\_alt}$, amplifying correction
579   errors. Moreover, the humidity and isotopic disparity between the air captured in the air bag
580   and lower-altitude ambient air widens with altitude, requiring more intensive corrections.
581   Consequently, both the uncertainty (Figs. 8 and 9) and the magnitude of the diffusion correction
582   (Fig. 7) increase with altitude.

583
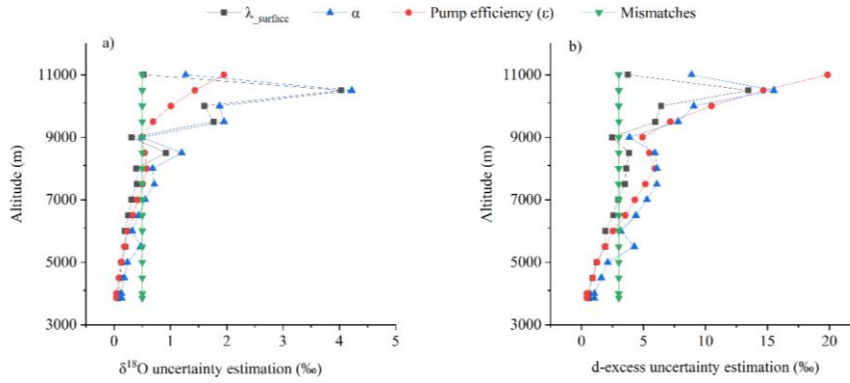
Figure 9 Mean uncertainty of $\delta^{18}O$ (a) and d-excess (b) with altitude for different sources.

584   On the contrary, errors pertaining to $\lambda_{\_surface}$ and α diminish at altitudes exceeding 10,500
585 meters. This phenomenon may be attributed to our sampling methodology. Although we
586 collected air samples in sequence from low to high altitudes, these samples were measured in
587 reverse order, from high to low altitudes. Consequently, samples taken from the highest
588 altitudes had the shortest storage durations, typically ranging from 10 minutes to two hours.
589 Additionally, we extended the sampling times with increasing altitude (Fig. A1). These
590 extended sampling periods and reduced storage durations help to partially offset the amplified
591 disparities observed between the raw and corrected profiles at higher altitudes. During the
592 drone-based sampling period, which lasted around 10-20 minutes, the external conditions
593 impacting the air bags were not the ground-level environmental values used in the model but
594 rather those of the vertical profile. However, the humidity at higher altitudes is lower than at
595 ground level, and the isotopic composition are closer to those inside the airbag. Consequently,
596 its impact on the airbag's internal conditions is less significant than suggested by using ground-
597 level environmental values. Therefore, the overestimated error in our model accounted for these
598 potential discrepancies.

599   The combined uncertainty from all sources, including $\lambda_{\_surface}$, α, pump efficiency (ε), and
600 model-experiment mismatches, results in a total uncertainty of approximately 1‰ for $\delta^{18}O$ and
601 8‰ for d-excess across 98% of the data. These ranges is acceptable when compared to the
602 substantial vertical variations we observed (~20‰ for $\delta^{18}O$ and ~100 ‰ for d-excess). Among
603 these sources, ε contributes the largest uncertainty, particularly at higher altitudes (Fig. 8), likely
604 due to the conservative uncertainty range we applied to account for potential reductions in
605 collected air mass at high altitudes. Additionally, $\lambda_{\_surface}$ and α and also contributes considerably
606 to the total uncertainty (Figs. 8 and 9). To mitigate this, we recommend conducting multiple
607 measurements to obtain an averaged value and performing repeated parameter validation to
608 ensure robustness.

4.5 **Comparison with Picarro measurements and satellite data**

611
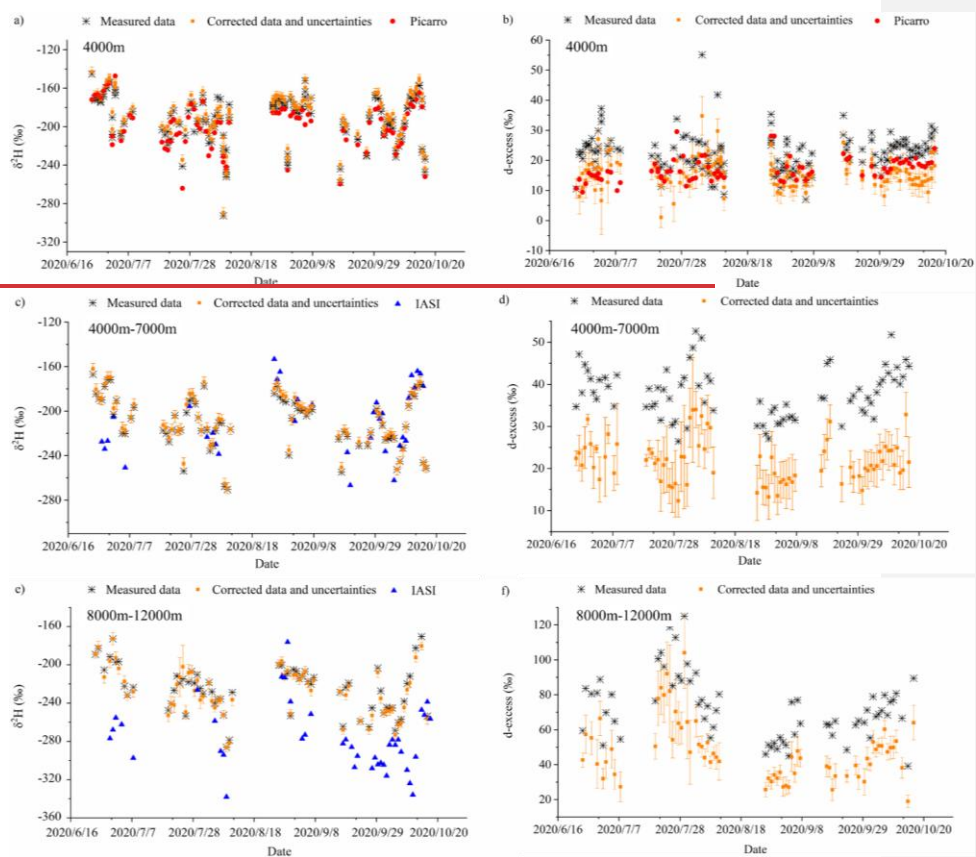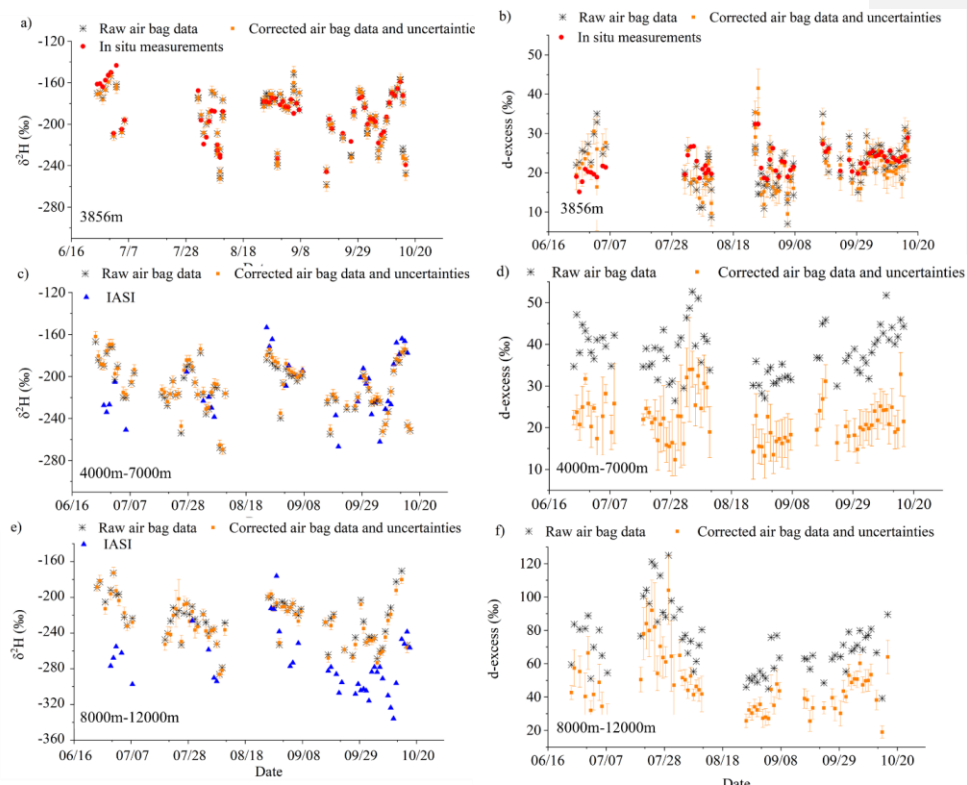
Figure 10 Time series comparison for δ^2H (a, c, e) and d-excess (b, d, f):

(a, b) Raw and corrected (with uncertainties) ~~altitude-averaged~~ instantaneous air bag measurements ~~from~~ at the surface (3856 m) ~~to 4000 m~~, compared with Picarro in-situ ~~surface-level~~ measurements at ~~3856 m~~the same altitude ~~taken by the Picarro~~, averaged over the sampling period ~~(legend: Picarro~~in situ measuremeents).

(c, d) Raw and corrected (with uncertainties) altitude-averaged air bag measurements from 4000 m to 7000 m, compared with satellite data (IASI).

(e, f) Raw and corrected (with uncertainties) altitude-averaged air bag measurements from 8000 m to 12000 m, compared with satellite data (IASI).

612   The left panel of Fig.10 (Figs. 10 a, c, and e) shows the comparison of raw and corrected
613 water vapor δ^2H measurements at different altitudes with in-situ surface-level measurements
614 on the Picarro or IASI satellite data at corresponding altitudes. There is ~~notable~~ agreement
615 between the raw measurements and corrected δ^2H ~~for altitudes 3856-4000m~~ and the in-situ
616 ~~water vapor~~ δ^2H observed directly by Picarro at ground level (3856m), with a mean absolute
617 error of 2.99 ‰ (Fig.10a, Fig.A3). The remaining minor differences can be attributed to the fact
618 that the Picarro in-situ observations are period-averaged, whereas the bag samples represent
619 instantaneous values. ~~~~To compare corrected measurements with independent observations at

设置了格式: 字体: 11 磅

higher altitudes, we refer to the IASI satellite dataset. We acknowledge that this comparison is qualitative, as satellite data represent vertical averages over layers defined by averaging kernels, and therefore differ in measurement footprints (both horizontal and vertical) and spatio-temporal sampling disparities (Shi et al., 2020). For most intervals, IASI satellite data closely matches raw and corrected δ^2H measurements for altitudes 4000–7000m. In the 8000–12000m range, IASI data is lower than δ^2H observations during certain periods, particularly June and September 2020. While the IASI data closely matches the observed δ^2H for all other periods in the 4000–7000 meter range, it is also lower in June 2020. A more quantitative analysis could be facilitated if an averaging kernel is used to smooth the observed profiles (Herman et al., 2014). All comparisons reflect consistent temporal variations.

The right panel of Fig.10 (Figs. 10 b, d, and f) shows the comparison of raw and corrected vapor d-excess measurements. As expected for near-surface sampling~~In the 4000m observations~~ (Fig. b), the differences between the bag samples and the ambient values are very small, and the impact of diffusion is minimal. Consequently, the applied corrections are also small. After correction, the a mean absolute error is 1.37 ‰. ~~raw d-excess in air bags were higher than corrected values due to kinetic fractionation during diffusion. After correction, d-excess decrease and are similar to in situ surface-level measurements on the Picarro at 3856 m.~~ For the 4000–7000m and 8000–12000m observations, no d-excess dataset is available for comparison (Fig. 10d and f). But our method provides a detailed assessment of all potential sources of error and quantifies the uncertainty range of the corrected data. As previously noted, raw d-excess are higher than corrected data due to kinetic fractionation. After correction, d-excess decreases. For the 8000–12000 m observations, the correction magnitude is smaller than at lower altitudes due to the shorter storage time of the air bags.

5   Conclusion

High spatial and temporal resolution water vapor isotope data are critical for understanding various hydrologic cycle processes. However, observations of vertical water vapor isotope profiles are scarce, particularly in the upper troposphere. Satellite-derived vapor isotope data are available only at limited vertical and temporal resolutions. Acquiring high-resolution water vapor isotope data, especially under conditions where direct measurements are difficult, has been a significant challenge for the water isotopes research community. This study demonstrates the potential of a drone-based air bag sampling method to overcome this challenge and offers solutions for evaluating air bag suitability and addressing air bag permeability.

While air bags offer the advantage of sample collection, their inherent permeability can affect the sealing integrity of the samples, leading to potential contamination. The permeability of airbag materials varies, with some exhibiting lower levels. We recommend prioritizing the use of glass containers and air bags with the lowest permeability for collecting water vapor using portable devices. Additionally, it is essential to conduct the permeability experiments described in this article before any experimental undertaking. This involves storing water vapor with known isotopic composition in the portable collection device for an extended period and

661 then re-measuring these values to assess or determine the device's permeability parameters.

662   To further address the permeability challenge, we developed a mathematical model to
663 evaluate and correct for diffusion and isotopic fractionation, ensuring the reliability of vapor
664 isotope measurements using air bags. Calibrated with parameters from laboratory experiments,
665 our correction model reconstructs the initial isotopic composition of sampled vapor by using
666 data from both the air bag and the surrounding environment, offers a potentialpractical solution
667 to the prevalent permeability challenges. This model was rigorously validated against
668 observational experiments conducted under varying conditions. We also applied this model to
669 drone-collected samples at various pressures. By estimating uncertainty and comparing
670 corrected data with in-situ surface-level measurements on the Picarro and satellite observations,
671 we validated the reliability and applicability of drone-based water vapor isotope measurements.

672   Our drone-based sampling system, combined with the diffusion model, effectively
673 addresses the limitations of traditional high-altitude water vapor measurement methods. It
674 meets the need for lightweight equipment while providing a more economical, efficient, and
675 flexible alternative to conventional approaches involving large aircraft, airships, and balloons.
676 This approach enables us to exploit the benefits of drone-based air bag sampling at high
677 altitudes and over long distances, while effectively mitigating its potential limitations. This
678 strategy significantly broadens its potential applications across various environments, thereby
679 enhancing the range and richness of data that can be gathered for water vapor isotope research.

680   This study was conducted under stable temperature and equal internal and external
681 pressures during storage. We acknowledge that a formulation based on partial pressure of water
682 vapor would be more general and could improve model applicability under varying temperature
683 and pressure conditions. Future work could extend the model to account for these factors.

684 ## Appendix A

Table $S1A1$ Summary of experiments: diffusion parameter quantification, model
validation and differences in experimental methods. $\lambda_{\_surface}$ denotes the water vapor
exchange coefficient at the surface, α refers to the fractionation coefficient of isotopes, q_0
represents the initial vapor humidity in the air bags, and q_e corresponds to the environmental
vapor humidity.

Experiment Number	Experimental purpose	Differences in experimental methods
No. 1	Quantification of $\lambda_{\_surface}$	Dry air in the air bags
No. 2	Quantification of α	Water vapor with known isotopic compositions in the air bags under the condition $q_0 = q_e$
No. 3	Diffusion model validation	Water vapor with varying isotopic compositions and humidity levels in the air bags

685
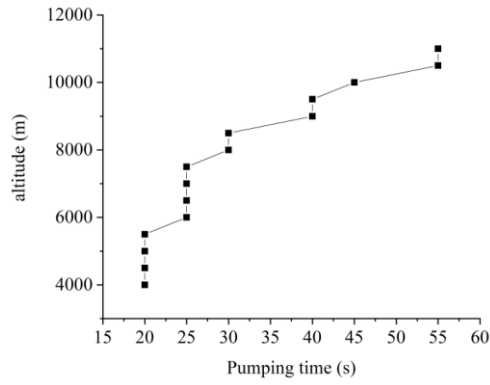
686
687   Figure ~~S1~~ A1 Sampling duration variation with altitude.
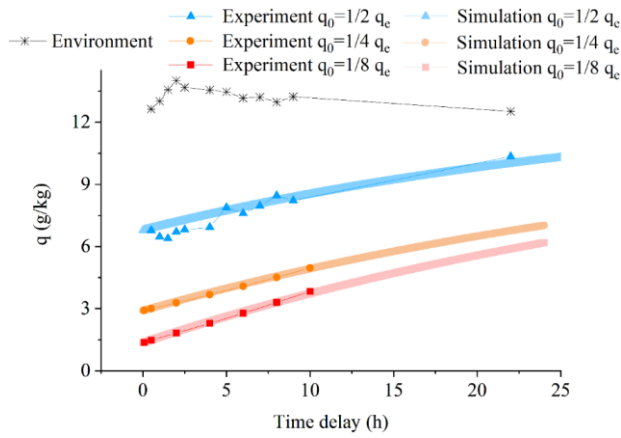
688
689   Figure ~~S2~~ A2 Comparison of humidity variation within the air bag over time in laboratory
690 permeability Experiments No.3 (markers) and diffusion model simulations (lines) for Figures
691 4 and 5. The experiments cover a range of initial humidities at t = 0 (q_0), from approximately
692   1/8 * q_e to 1/2 q_e, where q_e denotes environmental humidity.
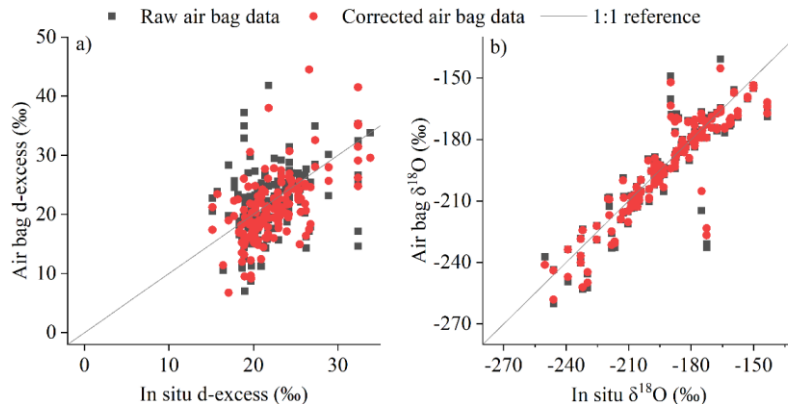
Figure A3 Comparison of raw and corrected air bag data with in situ observations averaged over the sampling period (1:1 reference shown)

Code availability

The diffusion modeling code, which simulates the evolution of water vapor isotopes in the airbag and corrects them to their initial values, is available at:

https://github.com/DishiWANG0608/Correcting-for-water-vapor-diffusion.git

Data availability

Data are available from the authors on request.

Video supplement

A video showcasing our field campaign on drone-derived water vapor isotope sampling up to the upper troposphere (11 km) during convective activity, including the workflow for airbag water vapor isotope sampling, is currently available upon request and will be publicly accessible in the near future. Please contact the corresponding author for access (di.wang@latmos.ipsl.fr).

Author contributions

D.W., C.R., and L.T. designed the research, established the subjects of the methodology, and performed the analysis; D.W. and D.Y. conducted the observations; G.B., S.F., H.P. and L.L. contributed to the establishment of methodologies, data calibration, and analysis; Y.S. provided assistance with the computing; All authors contributed to the discussion of the results

713 and the final article; D.W. drafted the manuscript with contributions from all co-authors.

Competing interests

715 The contact author has declared that none of the authors has any competing interests.

Acknowledgments

717 The authors gratefully acknowledge the Infrared Atmospheric Sounding Interferometer
718 (IASI) for providing spatiotemporal coverage of δ^2H retrieval. We thank Jiaping Xu, Mingjian
719 Chen, Le Chan, and Yao Yao for their irreplaceable help in the development of the drones. We
720 are grateful to the management of 99 Dragon, Mountain Laojun in Lijiang for facilitating the
721 field experiments. We thank Pengbin Liang and Jiangrong Tai for partially participating in the
722 field observations. We acknowledge Hans Christian Steen-Larsen and Harald Sodemann for
723 their discussions on the correction method. We acknowledge the use of OpenAI's ChatGPT to
724 assist in refining the language. This work was supported by the National Natural Science
725 Foundation of China (Grants No. 42401043 and U2202208), the fellowship from the China
726 Postdoctoral Science Foundation (Grant No.2025T180092), the Strategic Priority Research
727 Program of the Chinese Academy of Sciences (Grant No. XDB40000000), and the Science and
728 Technology Department of Yunnan Province (Grant No. 202201BF070001-021). Di Wang
729 acknowledges support from Chinese Scholarship Council and the Postdoctoral Fellowship
730 Program of China Postdoctoral Science Foundation (Grant No. GZC20241440). Siteng Fan
731 acknowledges support from the Marie Skłodowska-Curie Actions of European Research
732 Executive Agency (Grant No. 101064814) and the High Level Special Fund of Southern
733 University of Science and Technology (Grant No. G03050K001).

References

735 Ayliffe, L., Cerling, T., Robinson, T., West, A., Sponheimer, M., Passey, B., Hammer, J., Roeder, B.,
736 Dearing, M., Ehleringer, J., 2004. Turnover of carbon isotopes in tail hair and breath CO 2 of horses fed
737 an isotopically varied diet. Oecologia 139, 11-22.
738 Bony, S., Risi, C., Vimeux, F., 2008. Influence of convective processes on the isotopic composition
739 (δ18O and δD) of precipitation and water vapor in the tropics: 1. Radiative-convective equilibrium and
740 Tropical Ocean–Global Atmosphere–Coupled Ocean-Atmosphere Response Experiment (TOGA-COARE)
741 simulations. Journal of Geophysical Research: Atmospheres 113.
742 Bowen, G.J., Cai, Z., Fiorella, R.P., Putman, A.L., 2019. Isotopes in the Water Cycle: Regional-to
743 Global-Scale Patterns and Applications. Annual Review of Earth and Planetary Sciences 47.
744 Brienen, R.J., Schöngart, J., Zuidema, P.A., 2016. Tree rings in the tropics: insights into the ecology
745 and climate sensitivity of tropical trees. Tropical tree physiology: adaptations and responses in a
746 changing environment, 439-461.
747 Cerling, T.E., Wittemyer, G., Rasmussen, H.B., Vollrath, F., Cerling, C.E., Robinson, T.J., Douglas-

748 Hamilton, I., 2006. Stable isotopes in elephant hair document migration patterns and diet changes.
749 Proceedings of the National Academy of Sciences 103, 371-373.

750 Dansgaard, W., 1964. Stable isotopes in precipitation. Tellus 16, 436-468.

751 Fick, A., 1855. Ueber diffusion. Annalen der physik 170, 59-86.

752 Galewsky, J., Steen-Larsen, H.C., Field, R.D., Worden, J., Risi, C., Schneider, M., 2016. Stable isotopes
753 in atmospheric water vapor and applications to the hydrologic cycle. Reviews of Geophysics 54.

754 Gat, J.R., 1996. Oxygen and hydrogen isotopes in the hydrologic cycle. Annual Review of Earth and
755 Planetary Sciences 24, 225-262.

756 Ghosh, P., Brand, W.A., 2003. Stable isotope ratio mass spectrometry in global climate change
757 research. International Journal of Mass Spectrometry 228, 1-33.

758 Gralher, B., Herbstritt, B., Weiler, M., 2021. Unresolved aspects of the direct vapor equilibration
759 method for stable isotope analysis (δ 18 O, δ 2 H) of matrix-bound water: unifying protocols through
760 empirical and mathematical scrutiny. Hydrology and Earth System Sciences 25, 5219-5235.

761 Grootes, P.M., Stuiver, M., 1997. Oxygen 18/16 variability in Greenland snow and ice with 10(-3)-
762 to 10(5)-year time resolution. Journal of Geophysical Research-Oceans 102, 26455-26470.

763 Havranek, R.E., Snell, K.E., Davidheiser-Kroll, B., Bowen, G.J., Vaughn, B., 2020. The Soil Water
764 Isotope Storage System (SWISS): An integrated soil water vapor sampling and multiport storage system
765 for stable isotope geochemistry. Rapid Communications in Mass Spectrometry 34, e8783.

766 He, H., Smith, R.B., 1999. Stable isotope composition of water vapor in the atmospheric boundary
767 layer above the forests of New England. Journal of Geophysical Research Atmosheres 104, 11657-
768 11673.

769 Hendry, M., Schmeling, E., Wassenaar, L., Barbour, S., Pratt, D., 2015. Determining the stable
770 isotope composition of pore water from saturated and unsaturated zone core: improvements to the
771 direct vapour equilibration laser spectrometry method. Hydrology and Earth System Sciences 19, 4427-
772 4440.

773 Herbstritt, B., Gralher, B., Seeger, S., Rinderer, M., Weiler, M., 2023. Discrete in situ vapor sampling
774 for subsequent lab-based water stable isotope analysis. Hydrology and Earth System Sciences 27, 3701-
775 3718.

776 Herman, R., Cherry, J., Young, J., Welker, J., Noone, D., Kulawik, S., Worden, J., 2014. Aircraft
777 validation of Aura Tropospheric Emission Spectrometer retrievals of HDO/H 2 O. Atmospheric
778 Measurement Techniques 7, 3127-3138.

779 Hodges, J.T., Lisak, D., 2006. Frequency-stabilized cavity ring-down spectrometer for high-
780 sensitivity measurements of water vapor concentration. Applied Physics B 85, 375-382.

781 Johnson, L., Sharp, Z., Galewsky, J., Strong, M., Van Pelt, A., Dong, F., Noone, D., 2011. Hydrogen
782 isotope correction for laser instrument measurement bias at low water vapor concentration using
783 conventional isotope analyses: application to measurements from Mauna Loa Observatory, Hawaii.
784 Rapid Communications in Mass Spectrometry 25, 608-616.

785 Magh, R.-K., Gralher, B., Herbstritt, B., Kübert, A., Lim, H., Lundmark, T., Marshall, J., 2022.
786 Conservative storage of water vapour–practical in situ sampling of stable isotopes in tree stems.
787 Hydrology and Earth System Sciences 26, 3573-3587.

788 Michener, R., Lajtha, K., 2008. Stable isotopes in ecology and environmental science. John Wiley &
789 Sons.

790 Millar, C., Pratt, D., Schneider, D.J., McDonnell, J.J., 2018. A comparison of extraction systems for
791 plant water stable isotope analysis. Rapid Communications in Mass Spectrometry 32, 1031-1044.

792   Muccio, Z., Jackson, G.P., 2009. Isotope ratio mass spectrometry. Analyst 134, 213-222.

793   Rodgers, C.D., Connor, B.J., 2003. Intercomparison of remote sounding instruments. Journal of
794 Geophysical Research: Atmospheres 108.

795   Rozmiarek, K.S., Vaughn, B.H., Jones, T.R., Morris, V., Skorski, W.B., Hughes, A.G., Elston, J., Wahl,
796 S., Faber, A.-K., Steen-Larsen, H.C., 2021. An unmanned aerial vehicle sampling platform for atmospheric
797 water vapor isotopes in polar environments. Atmospheric Measurement Techniques 14, 7045-7067.

798   Salmon, O.E., Welp, L.R., Baldwin, M.E., Hajny, K.D., Stirm, B.H., Shepson, P.B., 2019. Vertical profile
799 observations of water vapor deuterium excess in the lower troposphere. Atmospheric Chemistry and
800 Physics 19, 11525-11543.

801   Shi, X., Risi, C., Pu, T., Lacour, J.l., Kong, Y., Wang, K., He, Y., Xia, D., 2020. Variability of isotope
802 composition of precipitation in the southeastern Tibetan Plateau from the synoptic to seasonal time
803 scale. Journal of Geophysical Research: Atmospheres 125, e2019JD031751.

804   Sprenger, M., Herbstritt, B., Weiler, M., 2015. Established methods and new opportunities for pore
805 water stable isotope analysis. Hydrological Processes 29, 5174-5192.

806   Steen-Larsen, H.C., Masson-Delmotte, V., Sjolte, J., Johnsen, S.J., Vinther, B.M., Bréon, F.M.,
807 Clausen, H.B., Dahl-Jensen, D., Falourd, S., Fettweis, X., 2011. Understanding the climatic signal in the
808 water stable isotope records from the NEEM shallow firn/ice cores in northwest Greenland. Journal of
809 Geophysical Research Atmospheres 116, 161-165.

810   Wassenaar, L., Hendry, M., Chostner, V., Lis, G., 2008. High resolution pore water δ2H and δ18O
811 measurements by H2O (liquid)– H2O (vapor) equilibration laser spectroscopy. Environmental science &
812 technology 42, 9262-9267.

813   West, A.G., Goldsmith, G.R., Brooks, P.D., Dawson, T.E., 2010. Discrepancies between isotope ratio
814 infrared spectroscopy and isotope ratio mass spectrometry for the stable isotope analysis of plant and
815 soil waters. Rapid Communications in Mass Spectrometry 24, 1948-1954.

816   West, J.B., Bowen, G.J., Dawson, T.E., Tu, K.P., 2009. Isoscapes: understanding movement, pattern,
817 and process on Earth through isotope mapping. Springer.

818   Worden, J., Bowman, K., Noone, D., Beer, R., Clough, S., Eldering, A., Fisher, B., Goldman, A.,
819 Gunson, M., Herman, R., Kulawik, S.S., Lampel, M., Luo, M., Osterman, G., Rinsland, C., Rodgers, C.,
820 Sander, S., Shephard, M., Worden, H., 2006. Tropospheric emission spectrometer observations of the
821 tropospheric HDO/H2O ratio: Estimation approach and characterization. Journal of Geophysical
822 Research-Atmospheres 111.

823   Yu, W., Tian, L., Ma, Y., Xu, B., Qu, D., 2015. Simultaneous monitoring of stable oxygen isotope
824 composition in water vapour and precipitation over the central Tibetan Plateau. Atmospheric Chemistry
825 and Physics 15, 10251-10262.

826

827